Physics of the Earth and Planetary Interiors 364 (2025) 107367

Contents lists available at ScienceDirect

Physics of the Earth and Planetary Interiors

journal homepage: www.elsevier.com/locate/pepi

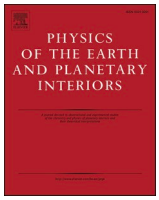

The impact of LLVPs on regional secular variation of the magnetic field☆

Hannah F. Rogers [a,*], Ciarán D. Beggan [b], Kathryn A. Whaler [c]

[a] School of Earth and Environment, University of Leeds, Woodhouse Lane, Leeds LS2 9JT, United Kingdom
[b] British Geological Survey, Research Avenue South, Edinburgh EH14 4AP, Scotland, United Kingdom
[c] University of Edinburgh, Grant Institute, James Hutton Road, Edinburgh EH9 3FE, Scotland, United Kingdom

ARTICLE INFO

Keywords:
Large low velocity provinces (LLVPs)
Regional models
Secular variation
Spherical Slepian functions
Spherical harmonics
Geomagnetic jerks

ABSTRACT

The Large Low Velocity Provinces (LLVPs) are two poorly understood features at the base of the mantle that are typically studied with seismology and explained using geodynamical models of Earth evolution. However, there are few insights from the geomagnetic perspective about how these mantle features affect main field generation, or if they perturb the motion of the Earth's outer core, without assuming their physical properties. In this study, we test three regional methodologies, namely pointwise estimate on a spatial grid, spherical harmonic analysis, and spherical Slepian functions, to separate secular variation (SV, the first time derivative of the magnetic field) in the areas beneath the LLVPs and their complement.

While all three methodologies have drawbacks and differences, our findings of the proportion of SV energy inside and outside LLVPs are robust. When inverting data from geomagnetic virtual observatories over the satellite era, the proportion of SV energy under the LLVPs is found to be between 12 % and 18 % of the total SV energy at the Earth's surface which is less than the percentage surface area of the LLVPs. However, the percentage of SV energy is larger than the corresponding surface area when separating the COV-OBS.x2 SV model, between 29 % and 37 % inside LLVPs at the Earth's surface and 33 % and 49 % at the core-mantle boundary (CMB). For both datasets the African LLVP contributes approximately 2.5 times the amount of SV energy as the Pacific LLVP at the Earth's surface but only around 1.3 times more energy at the CMB.

LLVPs show time-varying SV under their footprint on decadal timescales which, therefore, indicates that core flow varies significantly underneath them rather than being regions of stilted flow. As well as presenting a novel inversion methodology that inverts for a spherical Slepian model, rather than using spherical Slepian functions to separate an existing spherical harmonic model, we also show for the first time that the timings of geomagnetic jerks correspond with inflection points in the magnitude of spectral or spatial energy in regional SV models. We conclude that there is no evidence that SV is systematically suppressed beneath LLVPs.

1. Introduction

The deep Earth on or below the core-mantle boundary (CMB) is difficult to study due to the distance between observations taken at or above the surface and the properties and features that we wish to understand. One pair of unexplained features, first identified through seismic studies, at the base of the mantle are the Large Low Velocity Provinces (LLVPs), formerly Large Low Shear Velocity Provinces (LLSVPs). LLVPs are two equatorial and approximately antipodal low seismic velocity patches present at the base of the mantle covering around 25 % of the CMB surface (Koelemeijer, 2021). The seismic S-wave velocity is about 2.5 % lower and the P-wave velocity is 1–3 % slower than the global average wave speed at 2800 km depth (Ritsema et al., 2011; Frost and Rost, 2014; Ma and Tkalčić, 2024). These velocity anomalies are thought to be caused by a combination of temperature and compositional effects (McNamara, 2019; Koelemeijer, 2021; Richards et al., 2023).

While these low velocity provinces are approximately antipodal, their exact outlines are highly debated and little is presently known about their formation or internal structure (Doubrovine et al., 2016; Garnero et al., 2016; McNamara, 2019). Features at the top of the core and at the Earth's surface have been linked to the outline of LLVPs, such as the presence of Large Igneous Provinces, kimberlite structures, subduction margins, intra-plate magnetism, hot-spot traces, compositional

☆ This article is part of a Special issue entitled: 'SEDI 2024' published in Physics of the Earth and Planetary Interiors.

* Corresponding author.
E-mail address: h.f.rogers@leeds.ac.uk (H.F. Rogers).

https://doi.org/10.1016/j.pepi.2025.107367
Received 2 September 2024; Received in revised form 10 April 2025; Accepted 30 April 2025
Available online 9 May 2025

variation in volcanic melt (e.g. in ocean island basalts), dynamic topography on the CMB, plume structures in mantle dynamics, and stratification at the top of the outer core (e.g Kellogg et al., 1999; Garnero et al., 2005; Torsvik et al., 2010, 2014; Niu, 2018; Heyn et al., 2020; Yuan et al., 2023; Mound and Davies, 2023). Although LLVPs and their general properties have been widely discussed, it is uncertain what effect the regional heterogeneities have on the outer core beneath them. Instead, many parameters are linked by statistical correlation, seismic interpretations, and dynamo simulations with inhomogeneous boundary conditions (e.g Doubrovine et al., 2016; van Tent et al., 2020; Mound and Davies, 2023; Terra-Nova and Amit, 2024). Geochemical signatures of the LLVPs are contested but could give insights into their origin and whether they are recent and growing or were formed by primordial reservoirs and are essentially static on geological timescales (e.g Labrosse et al., 2007; Niu, 2018; Wang et al., 2020). Recent work has investigated whether the evolutionary history has led to different internal properties for the two LLVPs despite their similar seismic signatures (Yuan and Li, 2022b; Panton et al., 2025).

Since the LLVP seismic velocities may reflect enhanced temperatures, inhomogeneous heat flux boundary conditions at the CMB have been postulated as providing top down control on convection in the outer core. Models of convection can be split into two families depending on whether or not they consider magnetic forces, and whether they are kinematic or dynamic. Zhang and Gubbins (1992) showed that lateral variations in heat flux can influence surface flow in non-magnetic models, followed which Gibbons and Gubbins (2000) investigated the effect of equatorially anti-symmetric heat flux patterns on non-magnetic rotating convection. Gubbins et al. (2007) further correlated the geomagnetic field generated from dynamo models with the location of the tangent cylinder as well as LLVP features. Mound et al. (2019) added thermal variations at the CMB in a non-magnetic rotating convection model, which produced antipodal stratification aligned with the LLVP structures. Glatzmaier et al. (1999) first provided evidence of the effect of thermal structures on the reversing behaviour in numerical geodynamos; subsequent studies of long-term palaeomagnetic field behaviour include that of Davies et al. (2008) and Mound and Davies (2023). A full review of the effect of heat flux patterns on geodynamo models is given in articles by Amit et al. (2015) and Olson (2016). In general, equatorial cooling leads to a higher reversal frequency but it is difficult to see its influence on century to decadal timescales. Postulated links between long-lived features in the Earth's magnetic field and LLVPs have also been presented as evidence for top-down control on the geodynamo (e.g. Tarduno et al., 2015; Engbers et al., 2020). Whether these features solely apply a thermal forcing or whether there is a chemical exchange, dynamic topography or other effect on the core remains to be explored (Koelemeijer, 2021). It has long been observed that there is less secular variation (SV) generated by advection under the Pacific Ocean and the greatest amount of westward drift is recorded across the southern Atlantic and near the northern tangent cylinder (Jault et al., 1988; Holme, 2007; Baerenzung et al., 2016; Livermore et al., 2016; Mound and Davies, 2023), but there is no clear connection between LLVPs and these SV features.

In this paper, we investigate the effect of LLVPs' thermal forcing on geomagnetic field changes on timescales considerably shorter than those associated with reversals. We hypothesise that some regional influence of LLVPs on the flow of liquid at the core surface may be detectable in the SV as it is mostly generated through advection by the flow. As they are governed by mantle dynamics, we can regard the LLVPs as stable on the decadal timescales investigated in this study. To examine the regional influence of LLVPs we must consider SV models covering only part of the CMB surface.

Most investigations of Earth's core surface flow, magnetic field, and SV use spherical harmonics (Dahlen and Tromp, 1998; Winch, 2007; Holme, 2015) as they are a complete and compact set of orthogonal functions which can (in theory) define any scalar or vector function on the surface of a sphere. Such fields can be represented by spherical harmonics over a smaller region of a sphere and/or a region with a complex outline but this requires a large number of coefficients to preserve the spectral content of the signal (Simons et al., 2009). Also, the models will exhibit aliasing ('ringing') at the boundaries. We refer to unwanted aliasing and noise in models over part of the sphere (or its complementary region) as 'leakage'. The region that the signal is being confined to is analogous to the width of the box function in Fourier series and the leakage can be spatial (in terms of signal in the region complement) or spectral (by generating energy in the power spectrum not present in the original signal).

In this study we separate SV spatially and spectrally using three techniques: 1) point values from a spherical harmonic SV model, 2) spherical harmonic coefficient separation, and 3) spherical Slepian functions (often referred to as 'Slepian functions'). These techniques are chosen as they represent (i) purely spatial, (ii) purely spectral and (iii) 'spatial-spectral trade-off' methodologies, respectively. For (iii), we devise and implement a novel approach of inverting SV data for models confined to patches of the surface represented by spherical Slepian functions, as well as using these functions to localise existing SV models.

In this study, we invert for SV over patches of the Earth's surface and CMB using annual differences of the Geomagnetic Virtual Observatory (GVO) vector time-series constructed to best represent the core field from the CHAMP, Ørsted, Cryosat and Swarm satellites (Hammer et al., 2021a, 2021b). We also conduct regional separations of the SV Gauss coefficients from the COV-OBS.x2 model (Huder et al., 2020). This allows us to investigate the conjecture that variability in the SV power spectrum is indicative of the influence of the LLVPs on the flow at the core surface generating the SV.

In Section 2 we describe the spherical harmonic methodology for determining global models of SV followed by the three methodologies we have used for regional investigations in Section 3. In Section 4, we describe the datasets we use, Geomagnetic Virtual Observatories and COV-OBS.x2. Section 5 shows our results for each of the methodologies applied to GVO data for one time-step and we present the spatial/spectral signal over a surface separated into inside and outside LLVPs, described as 'decompositions'. Then we investigate the temporal variability over 23 years of satellite data (Section 6) and 1900–2020 from the COV-OBS.x2 model (Section 7). We conclude in Section 8 by considering the geophysical implications of these results and potential further work.

2. Global models of secular variation

The measured magnetic field contains contributions from numerous internal and external field sources. We will consider only those originating in the core for which the field, **B**, can be expressed in spherical coordinates (r, θ, ϕ) as the gradient of a scalar potential (V):

$$V(r,\theta,\phi) = R_E \sum_{l=1}^{L} \sum_{m=0}^{l} \left(\frac{R_E}{r}\right)^{l+1} \left[g_l^m \cos(m\phi) + h_l^m \sin(m\phi)\right] P_l^m(\cos\theta) \qquad (1)$$

R_E is the reference radius, normally the radius of the Earth, $P_l^m(\cos\theta)$ are associated Legendre polynomials, and the coefficients g_l^m and h_l^m are spherical harmonic (Gauss) coefficients representing the field at radius R_E. These coefficients are determined from the measured components of **B** by, for example, least squares fitting to a maximum degree, L, dependent on the noise and the data distribution. The spherical harmonic degree l is related to spherical wavenumber or lengthscale. The same expression can be used to represent the rate of change of the field, or SV, $\dot{\mathbf{B}}$, with coefficients $\dot{g}_l^m$ and $\dot{h}_l^m$. We introduce Schmidt quasi-normalised spherical harmonics $Y_l^m(\theta,\phi) = P_l^m(\cos\theta)e^{im\phi}$. Their orthogonality over the sphere gives:

$$\oint Y_l^{m^*}(\theta,\phi) Y_{l'}^{m'}(\theta,\phi) d\Omega = \begin{cases} \frac{4\pi}{2l+1}, & \text{when } l = l', m = m' \\ 0, & \text{otherwise} \end{cases} \qquad (2)$$

where * denotes complex conjugate. This provides an alternative means to derive values of the Gauss coefficients. Rewriting eq. (1) for the SV as

$$\dot{V}(r,\theta,\phi) = R_E \sum_{l=1}^{L}\sum_{m=0}^{l}\left(\frac{R_E}{r}\right)^{l+1} \dot{f}_l^m Y_l^m(\theta,\phi) \tag{3}$$

where

$$\dot{f}_l^m = \dot{g}_l^m + i\dot{h}_l^m, \tag{4}$$

the radial component of SV is given by

$$\dot{B}_r(r,\theta,\phi) = \sum_{l=1}^{L}\sum_{m=0}^{l}\left(\frac{R_E}{r}\right)^{l+2}(l+1)\dot{f}_l^m Y_l^m(\theta,\phi). \tag{5}$$

Hence using eq. (2) we have

$$\dot{f}_l^m = \frac{1}{4\pi}\left(\frac{r}{R_E}\right)^{l+2}\frac{2l+1}{l+1}\oint \dot{B}_r(r,\theta,\phi)Y_l^m(\theta,\phi)d\Omega. \tag{6}$$

The linear relationship between orthogonal component SV data collected at or near the Earth's surface and a spherical harmonic model of them can be written

$$\mathbf{d} = \mathbf{A}\dot{\mathbf{g}}, \tag{7}$$

where $\mathbf{A}$ is a matrix constructed from gradients of the potential (Eq. (1)), $\dot{\mathbf{g}}$ is a vector of the Gauss coefficients representing the SV, and $\mathbf{d}$ is the vector of observed SV in X, Y, Z or r, θ, ϕ components. A typical inversion produces a spherical harmonic SV model by a Moore-Penrose (regularised least-squares) inversion (e.g. Beggan and Whaler, 2008) that can be evaluated on the CMB or at Earth's surface:

$$\dot{\mathbf{g}} = \left(\mathbf{A}^\mathbf{T}\mathbf{C}\mathbf{A} + \lambda\mathbf{D}_\mathbf{SV}\right)^{-1}\mathbf{A}^\mathbf{T}\mathbf{C}\mathbf{d}, \tag{8}$$

where $\mathbf{C}$ is the data covariance matrix. Damping dependent on spherical harmonic degree is included to force convergence of the solution. λ is a damping parameter which determines the relative importance of fitting the data and the amount of spatial complexity of the SV model. We choose two values of λ (one for CMB and one for Earth's surface) that produce global SV models that match the results of the CHAOS-7 model (Finlay et al., 2020). The same values of λ are used in the regional investigations, and $L = 14$ throughout this study. The matrix $\mathbf{D_{SV}}$ is diagonally degree dependent and minimises the root mean square radial SV over the surface (Lowes, 1966; Mauersberger, 1956; Maus, 2008):

$$\mathbf{D_{SV}} = \frac{(l+1)^2}{(2l+1)}. \tag{9}$$

In addition, we use SV coefficients (also to degree and order 14) from the COV-OBS.x2 model, as described in Section 4.2.

3. Methodology for regional investigations

We wish to examine the effect of LLVPs on time series of the SV. We compare three methodologies to separate or localise SV into the regions bounded by LLVPs and their complement: (i) a spatial grid of magnetic values, (ii) spherical harmonic coefficient separation and (iii) spherical Slepian decomposition. These should represent the optimal (i) spatial, (ii) spectral and (iii) spatio-spectral decompositions, respectively. We assess our attempts at separation in the spatial domain from maps of the radial SV, and in the spectral domain from the power spectra, the radial SV energy as a function of spherical harmonic degree (Lowes, 1966):

$$S_l = \frac{(l+1)^2}{2l+1}\left(\frac{R_E}{r}\right)^{2l+4}\sum_{m=0}^{l}\left(\dot{g}_l^m\right)^2 + \left(\dot{h}_l^m\right)^2 \tag{10}$$

as well as the total radial component energy

$$\int_{\mathcal{R}}\dot{B}_r^2 d\Omega = \sum_{l=0}^{L} S_l, \tag{11}$$

where $\mathcal{R}$ is the region under consideration, or the full sphere. In eq. (10), the coefficients $\left(\dot{g}_l^m, \dot{h}_l^m\right)$ will represent those for $\mathcal{R}$ or the global model, as appropriate. The spatial separation (i) does not provide any information about the spectral content of the signal, but we can estimate the total radial energy in each region from the grid values. For an ideal separation, the sum of the regional spectral energies should equal the initial global spectral energy and all of the regional signal should be solely contained within the boundary of the region of interest.

The boundaries used to define the regions of investigation are shown in Fig. 2 and are a smoothed outline of the median location of LLVPs identified from studies such as that of Doubrovine et al. (2016). We remind the reader that we only consider the lateral extent of the LLVPs on a spherical shell and assume no depth or physical properties of the LLVPs. The African and Pacific LLVPs will be treated separately as well as together.

3.1. Spatial grid

The simplest methodology to investigate the difference in the character of the SV inside and outside the LLVPs is through its energy content calculated from a spatial grid of point values at the radius of interest. From a global spherical harmonic model of SV (obtained using Eq. (8)), we compute the radial SV values on an equal 1° colatitude and longitude area grid and determine whether each grid point lies within or outside the LLVP and then calculate the regional energy. We also calculate the percentage of the energy over the full spherical surface that is contributed by the region, and compare it to the percentage of the surface area that the region covers. The mathematical representation of this is to include only the 'inside' or 'outside' region ($\mathcal{R}$) points and to calculate the energy from these (on a $1^\circ \times 1^\circ$ grid) as:

$$S_{SG} = \frac{1}{N_\mathcal{R}}\sum \sin(\theta_\mathcal{R})\dot{B}_r(\mathcal{R})^2, \tag{12}$$

where $N_\mathcal{R}$ is the number of points in the region and θ is colatitude. The $\sin(\theta_\mathcal{R})$ factor accounts for the smaller surface area of a grid cell in the polar regions. However, this technique does not provide any information about the spectral content of the signal.

3.2. Spherical harmonic analysis

One way to overcome the lack of spectral information from the pointwise methodology is to calculate a spherical harmonic model representing the SV only in the region of interest. To find such a regional model, grid values from a global spherical harmonic inversion or the COV-OBS.x2 model are set to zero in areas outside the region of interest; this represents a 'hard' geographical boundary between the region of interest and its complement that generally leads to unwanted aliasing, and the resulting contamination of the spatial signal within the region of interest. The mathematical representation of this is:

$$S_{SH} = \frac{l+1}{2l+1}\left(\frac{R_E}{r}\right)^{2l+4}\sum_{m=0}^{l}\left(\dot{g}_l^m(\mathcal{R})\right)^2 + \left(\dot{h}_l^m(\mathcal{R})\right)^2, \tag{13}$$

where $\mathcal{R}$ is the region of interest. The Gauss SV coefficients are obtained from eq. (6) where $\dot{B}_r$ is set to 0 unless the position (θ, ϕ) is within $\mathcal{R}$.

3.3. Spherical Slepian functions

Spherical Slepian functions localise a spatio-spectral signal by maximising the signal within a region of interest while remaining orthogonal

both across the sphere (as with spherical harmonics) and within the region. Slepian functions are ordered by their contribution to the region of interest. The 'spatial-spectral trade-off' is achieved when the signal is concentrated within the region of interest with minimal signal outside of it (Dahlen and Simons, 2008). Spherical Slepian functions have previously been applied to determining local gravitational changes arising from large earthquakes or ice loss, the spectral structure of the cosmic microwave background radiation, the study of geodetic datasets containing spatial gaps, and to investigate the crustal magnetic field (Dahlen and Simons, 2008; Simons et al., 2009; Harig and Simons, 2012; Beggan et al., 2013; Kim and von Frese, 2017; Plattner and Johnson, 2021). LLVPs have a moderately simple outline in plan view but are not a spherical cap, requiring the investigation of their properties using spherical Slepian functions with a non-analytical solution.

The simplest case of the generation of spherical Slepian function models is the application to spherical harmonic models of scalar potential fields (Simons et al., 2006; Dahlen and Simons, 2008). Spherical Slepian functions on a unit sphere provide a different set of orthonormal basis functions, which are linearly related to spherical surface harmonics by the expression

$$g_\alpha(\theta,\phi) = \mathbf{g}_\alpha \cdot \mathbf{Y}(\theta,\phi). \tag{14}$$

where $\mathbf{Y}$ is a vector of spherical harmonics Y_l^m up to degree and order L and α labels the mutually orthogonal eigenvectors of the Slepian coefficients in $\mathbf{g}$. This means that a spherical Slepian solution can be projected onto the spherical harmonic basis to provide the equivalent Gauss coefficients, which are then used for plotting and power spectra calculation. The spherical Slepian decomposition determines a complete set of basis functions for a given region of the spherical surface, which are subsequently ordered in terms of their contribution to that region (essentially how concentrated each eigenvector is within the region, $\mathcal{R}$) and, finally, split into the 'in' and 'out' of region sections as two distinct domains:

$$\mathbf{G}^\top \mathbf{Y}(\theta,\phi) = \begin{bmatrix} \mathbf{G}_{in}^\top \mathbf{Y}(\theta,\phi) \\ \mathbf{G}_{out}^\top \mathbf{Y}(\theta,\phi) \end{bmatrix} = \begin{bmatrix} g_1(\theta,\phi) \\ \vdots \\ g_K(\theta,\phi) \\ g_{K+1}(\theta,\phi) \\ \vdots \\ g_{(L+1)^2}(\theta,\phi) \end{bmatrix} = \begin{bmatrix} \mathbf{g}_{\text{in}}(\theta,\phi) \\ \mathbf{g}_{\text{out}}(\theta,\phi) \end{bmatrix}. \tag{15}$$

K denotes the last element of the functions primarily concentrated in the first domain (in this case 'in'), and $K+1$ denotes the first function for the second ('out') domain. K can be set to be any value between 1 and $L(L+2)$ but generally is chosen to be at the point where the ordered functions contribute 50 % of their energy to inside the region of interest, also called the 'Shannon Number' (Simons, 2010). Previous work has shown that choosing K to be the 'Shannon Number' gives similar results to choosing K to be proportional of the surface area of the region of interest on the sphere (Simons et al., 2006; Beggan et al., 2013). We attempted separations using both the Shannon Number and choosing K to be proportional to the surface area and found no major difference in the results for the two choices.

The matrix $\mathbf{G}$ is constructed by optimization to localise the solution over a specified region (or its complement) for a given maximum spherical harmonic degree, L, while the functions remain orthonormal over both the region, $\mathcal{R}$, and the whole sphere, Ω. Therefore, the scaled eigenfunctions depend only on the maximum degree and the area and shape of the region on the sphere (Simons et al., 2006). Further details about the construction of scalar spherical Slepian functions are given by Simons (2010) and Rogers et al. (2019).

Each column of $\mathbf{G}$ contains one eigenvector and Λ is a diagonal matrix with the corresponding eigenvalues for the Gram matrix of energy ($\mathbf{E}$) in $\mathcal{R}$:

$$\mathbf{E} = \int_{\mathcal{R}} \mathbf{Y}(\theta,\phi)\mathbf{Y}^T(\theta,\phi)d\Omega = \int_{\mathcal{R}} \begin{bmatrix} Y_1^1 Y_1^1 & \cdots & Y_1^1 Y_{L(L+2)}^{L(L+2)} \\ \vdots & \ddots & \vdots \\ Y_{L(L+2)}^{L(L+2)} Y_1^1 & \cdots & Y_{L(L+2)}^{L(L+2)} Y_{L(L+2)}^{L(L+2)} \end{bmatrix} d\Omega, \tag{16}$$

$$\mathbf{EG} = \mathbf{G}\Lambda, \tag{17}$$

$$\Lambda = diag\left(\lambda_1, \cdots, \lambda_\alpha, \cdots, \lambda_{(L+1)^2}\right). \tag{18}$$

To maximise the energy ratio within a region, we find the solution to:

$$\lambda = \frac{\int_{\mathcal{R}} g^2(\theta,\phi)d\Omega}{\int_{\Omega} g^2(\theta,\phi)d\Omega} = \text{maximum}. \tag{19}$$

All of the eigenvalues of $\mathbf{E}$ are positive (or zero) and real, and its eigenvectors are orthogonal, which makes $\mathbf{G}$ unitary.

For an optimal signal decomposition, the result of summing the basis functions for the 'in' and 'out' regions will be identical to the input function and the 'in' region will be fully recreated by using all coefficients up to the specified value of K with no signal outside the region of interest. Such a decomposition is more difficult when a band limited signal is decomposed because the bandwidth, L, provides a fixed spatial resolution. Therefore, the resulting decomposition from a model with restricted spherical harmonic degree is more likely to have strong leakage, identified by smearing and signal appearing outside the region of interest (Simons, 2010).

Here, we have developed a new approach by incorporating the spherical Slepian functions into the Moore-Penrose (regularised least-squares) data inversion given by Eqs. (7)–(8). This allows us to invert directly for a localised model in the Slepian basis, rather than performing the Slepian separation of a spherical harmonic model. If we use all the Slepian basis functions, then the model will be identical to that obtained with usual spherical harmonic inversion. Therefore, starting from eq. (7), we can write:

$$\mathbf{d} = \mathbf{A}\dot{\mathbf{g}} = \mathbf{AGG}^T\dot{\mathbf{g}} \tag{20}$$

since $\mathbf{G}$ is unitary. After substituting $\mathbf{AG} = \mathbf{M}$ and $\mathbf{G}^T\dot{\mathbf{g}} = \mathbf{N}$ into the standard inversion we obtain

$$\mathbf{d} = \mathbf{MN} \tag{21}$$

$$\mathbf{N} = \left(\mathbf{M^T C M} + \mathbf{D_{SV}}\right)^{-1}\mathbf{M^T C d} \tag{22}$$

Damping is incorporated into the Slepian basis inversion by pre- and post-multiplying $\lambda\mathbf{D}$ by $\mathbf{G^T}$ and $\mathbf{G}$ respectively. We can then factorise and convert this back to the spherical harmonic basis for power spectrum calculation, plotting and comparing the model to the global spherical harmonic inversion:

$$\mathbf{G}^T\dot{\mathbf{g}} = \left(\mathbf{G}^T\left[\mathbf{A}^T\mathbf{C}\mathbf{A} + \lambda\mathbf{D_{SV}}\right]\mathbf{G}\right)^{-1}\left[\mathbf{AG}\right]^T\mathbf{C d} \tag{23}$$

$$\dot{\mathbf{g}} = \mathbf{G}^{-1}\left(\left(\mathbf{G}^T\left[\mathbf{A}^T\mathbf{C}\mathbf{A} + \lambda\mathbf{D_{SV}}\right]\mathbf{G}\right)^{-1}\left[\mathbf{AG}\right]^T\mathbf{C d}\right). \tag{24}$$

We restrict the number of Slepian eigenfunctions to complete a regional decomposition between 'in' (1 to K functions) and 'out' ($K+1$ to $L(L+2)$ functions).

$$\dot{\mathbf{g}}_{in} = \mathbf{G}_{1:K}^{-1}\left(\left(\mathbf{G}_{1:K}^T\left[\mathbf{A}^T\mathbf{C}\mathbf{A} + \lambda\mathbf{D_{SV}}\right]\mathbf{G}_{1:K}\right)^{-1}\left[\mathbf{AG}_{1:K}\right]^T\mathbf{C d}\right). \tag{25}$$

4. Secular variation data

The data used in this study are from two sources: (1) satellite data mimicking the temporal variation at a fixed location using the GVO technique, and (2) the Gauss SV coefficients from the COV-OBS.x2 geomagnetic model.

4.1. Geomagnetic virtual observatories

The GVO technique produces a time-series at a fixed location at satellite altitudes in a similar manner to those at ground observatories. Originally proposed by Mandea and Olsen (2006), and here using the methodology of Hammer et al. (2021a), GVOs combine all measured magnetic readings made in a given time within equal-area spaced cylinders of 700 km radius to an estimate at a central point at the mean satellite altitude (the GVO), using a cubic polynomial expansion of the potential to account for the along-orbit positions of the satellite within the cylinder of interest. SV is calculated by taking annual first differences of the GVO data. GVO data have been used for data assimilation experiments using statistics from geodynamo simulations and for studying core flow (e.g. Barrois et al., 2018; Kloss and Finlay, 2019; Whaler et al., 2022). For this study we have used the 4-monthly CHAMP, Cryosat and Swarm GVO dataset covering January 2001 to January 2023 (Hammer et al., 2021a, 2021b). We take R_E in Eq. (1) to be Earth's surface radius plus the mean satellite height.

4.2. COV-OBS.x2

The COV-OBS.x2 model is the most recent update to a magnetic model of the Earth describing the main field from 1840 to 2020 (Huder et al., 2020). The COV-OBS.x2 main field model is produced from ground-based observatories as well as CHAMP and Swarm satellite data, and historical (1840–1980) surveys (Huder et al., 2020). The model consists of Gauss coefficients at the Earth's surface with a spline dependence on time, as well as an estimate of their uncertainties based on temporal cross-covariances. The SV is calculated by time differentiating the splines. The COV-OBS models are well established and have been used as a candidate for the IGRF-13 (Alken et al., 2021a, 2021b). Over the satellite era, COV-OBS.x2 agrees well with other models of the field such as CHAOS-7 (Finlay et al., 2020). The Gauss coefficients $\dot{\mathbf{g}}$ are used directly in the pointwise and spherical harmonic separations and are separated using Eq. (15) for the spherical Slepian decompositions.

5. Regional separation of SV for a single GVO Timestep

We first illustrate the three methodologies by separating models inverted from GVO SV into the LLVPs and their complement for one timestep (September 2015) at the Earth's surface and at the CMB. In Section 6 we repeat the same inversion methodology of GVO SV data over the full satellite era (2000−2023) and in Section 7 we investigate the SV beneath LLVPs and their complement by separating the COV-OBS.x2 field model over 1900–2020. The SV on the CMB is more complex with enhanced small length-scale features, and its energy spectrum increases with spherical harmonic degree with greater downward continuation. The 'Sum of Separation' is obtained by adding results from the African LLVP, Pacific LLVP and outside the LLVPs, which can be compared to the input models.

5.1. Spatial grid

We extract values of the radial SV at each $1^\circ \times 1^\circ$ point grid to calculate the local energy in each region using Eq. (12). Fig. 1 shows the total energy for the GVO global spherical harmonic model, its division between inside the LLVPs and outside the LLVPs, and the separation into energy in the African and Pacific LLVPs separately at Earth's surface (a) and the CMB (b) and Table 1 compares the percentage of radial SV energy at the surface and CMB to the percentage of the sphere that the region covers.

Whether calculated at the surface or the CMB, the summed energy of the African LLVP, Pacific LLVP and outside of the LLVPs equals the global energy. We find that the partition of energy at the Earth's surface and the CMB are radically different, partly due to the spherical harmonic degree dependence of upward and downward continuation between the Earth's surface and CMB. The Pacific LLVP energy changes the most on downward continuation as it contributes around 7 % less average SV energy than its proportional surface area at the surface but 4 % greater

Table 1
Proportion of surface area, the radial SV energy at Earth's surface and the CMB for each of the LLVPs and their complements calculated by pointwise summation of numerical values when considering a global spherical harmonic model derived from Swarm GVO data in September 2015.

	Surface Area	Surface Energy	CMB Energy
Inside LLVPs	21.8 %	12.0 %	31.9 %
Outside LLVPs	78.2 %	88.0 %	68.1 %
African LLVP	11.9 %	9.3 %	18.0 %
Pacific LLVP	9.9 %	2.6 %	13.9 %
Sum	100 %	100 %	100 %

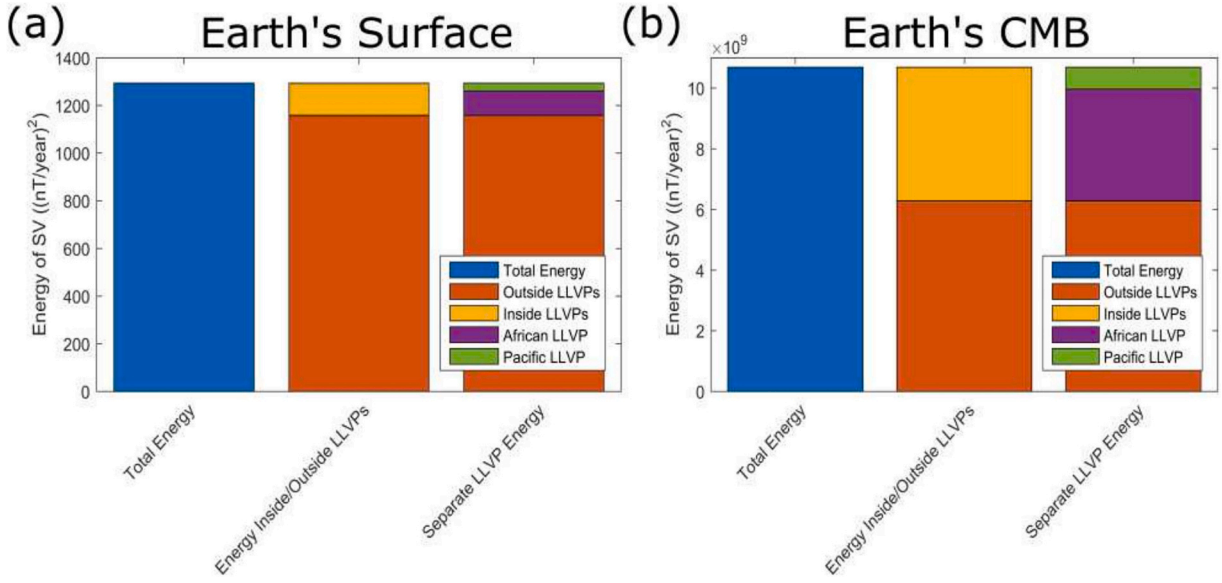

Fig. 1. The energy of the radial SV for September 2015 calculated from spatial grid of points lying within their respective regions from a global SH model derived from Swarm GVOs at the Earth's surface (left) and Core-Mantle Boundary (CMB, right).

than its proportional surface area at the CMB. The African LLVP energy is also proportionally higher at the CMB. The percentage SV energy outside the LLVPs (68 %) is smaller than expected from its surface area (81%) at the CMB, whereas it is larger than expected at the Earth's surface.

5.2. Spherical harmonic separation

The result of separating the SV using spherical harmonics can be seen in Fig. 2. In this and all subsequent maps we illustrate the results with the radial SV component. We use the global spherical harmonic basis functions but separate the signal into the region of interest and its complement by integrating the function described only within the region of interest over the whole sphere. The sums of the spatial maps for the separate LLVPS (panels e and f, and l and m for Earth's surface and CMB respectively) are equal to the spatial maps for the regions inside the LLVPs considered together (panels c and j), and maps from the global spherical harmonic model (panels a and h) and the sums of the separations (panels b and i) are exactly equal. There is no difference between the global spherical harmonic inversion and the sum of the separated parts. Therefore, the separations appear to be 'ideal' in the spatial domain according to our criterion.

However, the separations do not appear to be 'ideal' in the spectral domain. In Figs. 2(g) and 2(n), the dashed red lines representing the sums of the spectra of the individual regions do not match the solid black line, the power spectra of the global model. Although degree 2 spherical harmonics dominate both the outline of the LLVPs and the deep mantle seismic velocity variation, they do not have an anomalous contribution to the radial SV energy. Fig. 2(g) agrees with the results from the spatial grid methodology (Section??) and shows that the the area outside of the LLVPs generates more SV energy than inside the LLVPs at Earth's surface, but we can gain further insight from degree-dependence. The African LLVP contributes considerably more energy than the Pacific LLVP for all degrees except degree 1, where their energy is comparable.

At the CMB (Fig. 2(n)), the low degree (large spatial-scale) SV energy is over-estimated compared to the global spherical harmonic inversion in all of the individual regions. The sum of the decomposition is only similar to the global spherical harmonic inversion for spherical harmonic degrees higher than 10, and the area outside LLVPs contributes almost all of the energy to the summed contribution. This is somewhat counter intuitive to the total radial energy across all degrees underestimating the global spherical harmonic inversion. This is partly due to the spectra of SV being more blue at the Earth's core surface and red at the Earth's surface. The percentage of accumulated SV energy in degrees one to five compared to one to fourteen is 86.4 % at the Earth's surface but only 1.3 % at the CMB. It may be that some of the large-scale spectral energy has been restructured to fit within the complex outline of the LLVPs, resulting in a lower energy at low degrees and a higher energy at high degrees.

5.3. Spherical Slepian functions

Unlike the previous two methodologies, the separation using spherical Slepian functions is a spectral-spatial trade-off and allows for some leakage of the signal in the region of interest into its complementary region, shown in Fig. 3. Immediately, it can be seen that there is almost no signal modeled within the LLVPs (panels j, i and m) for inversion at CMB radius. This extreme application of altitude-cognizant Slepian functions (50 % of the observation radius compared to previous applications of about 6 % (Plattner and Simons, 2015)) shows that there may be a limit to depth of their practical utility, especially when combined with a bandlimited (low maximum spherical harmonic degree) signal. The outside LLVPs spatial map (panel k) shows stronger SV energy than the spherical harmonic case and overestimates the spectral energy at all spherical harmonic degrees (panel n). Fig. 3(n) also shows that the spectral signal inside the LLVPs (separate or not) is particularly low at the highest spherical harmonic degrees (small-scale features). The summation of the separated regions (panel i) looks very different to that from the global spherical harmonic inversion (panel h) and we have not been able to recreate features in the global spherical harmonic inversion within the separated regions.

At Earth's surface, the spherical Slepian decompositions are less spatially smooth than the spherical harmonic separations (shown in Fig. 2) as the spatio-spectral trade-off allows signal to escape the region. The areas closest to the region edges are most affected by a dappled signal created by this 'ringing' effect, such as at the eastern edge of the African LLVP in Fig. 3(c-e). This ringing generates strong variations of opposite polarity near to each other, especially where the region edges have a more pointed corner or are close to each other. The summed regions (panel b) no longer perfectly match the global model (panel a) and, therefore, fail to achieve a perfect spatial separation, although features within the regions visible in the global model are recreated.

Another difference between the spherical harmonic and the Slepian separation is that the separations using the individual LLVP outlines (panels e and f) vary in structure compared to the decompositions of both LLVP regions (panel c). As the unitary matrix, $\mathbf{G}$, is only dependent on the region outline and the maximum spherical harmonic degree, the difference must be due to the different region edges and the reduction in the number of eigenfunctions used to describe radial SV within the regions. There is more small scale structure in the 'inside' LLVPs (panel c) compared to the individual regions, especially for the Pacific LLVP (panel f). The summation of the individual (panels e and f) or 'inside' LLVPs (panel c) with the outside LLVPs (panel d) gives two different results. Regardless of the choice of 'inside' LLVPs and adjustments to the cut-off between 'in' and 'out', the spherical Slepian functions do not produce a good recreation of the global spherical harmonic model when the individual regions are summed. This indicates that there is insufficient bandwidth available (up to our maximum spherical harmonic degree) to capture the complexities of the region with the spherical Slepian functions.

Despite differences when considering the outline of individual LLVPs (panels e and f) or both together (panel c), there are robust features that are found when conducting the Slepian separations. The western and south-eastern edges of the African LLVP have a strongly positive SV but it is weaker and negative in the central region. Meanwhile SV inside the southern Pacific LLVP is consistently weakly negative but inside the northern half of the Pacific LLVP it is highly variable depending on the number of eigenfunctions used for the Slepian separation. The region outside the LLVPs better reproduces the field in the northern hemisphere compared to the southern hemisphere, reflecting the effect of the more complex shape of the region.

The power spectra of the spherical Slepian decomposition at the Earth's surface (shown in Fig. 3(g)) are flatter than those of the spherical harmonic separation. The spectra for 'outside' LLVPs are a similar shape to those of the spherical harmonic inversion for all degrees, but the spectra for inside the LLVPs fail to capture the higher energy at the lowest spherical harmonic degrees. The energy at lowest spherical harmonic degrees may be distributed to the higher order degrees, and we see the same splitting behaviour of energy into oppositely signed Slepian coefficients as when decomposing existing spherical harmonic models of core surface flow (Rogers et al., 2019). The Pacific LLVP has lowest SV energy across all spherical harmonic degrees but, curiously, the energy 'inside' LLVPs is less than that in the Pacific LLVPs for degrees three and seven. This highlights the effect of different outlines on the construction of the Slepian localisation matrix.

To understand the difference when considering the LLVPs together or individually, and the poor separation of the SV at the CMB, we plot the Slepian eigenfunctions and their footprint on the surface of the globe at the Earth's surface and at the CMB in Fig. 4. At the Earth's surface, the eigenfunctions are well constrained to the region and the choice of K always corresponds to approximately 50 % energy contribution with minimal leakage outside the region edge. The bottom row shows the

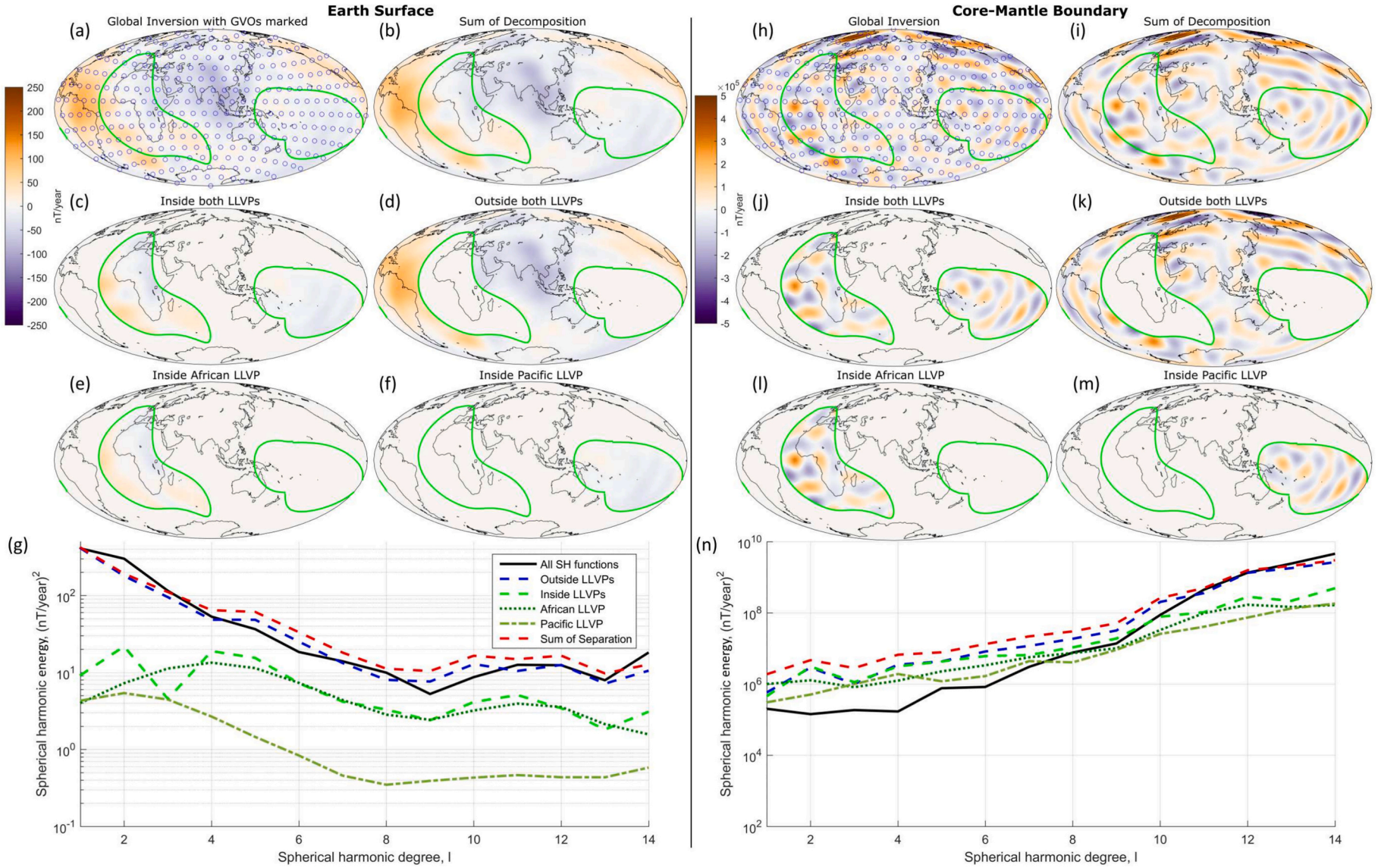

Fig. 2. Regional separation of radial SV inverted from Swarm GVOs using spherical harmonic methodology into inside the LLVPs, outside the LLVPs, the African LLVP, and the Pacific LLVP. (Left) At the Earth's surface and (right) at the CMB. Bottom panels of each plot are the power spectra for the separations above.

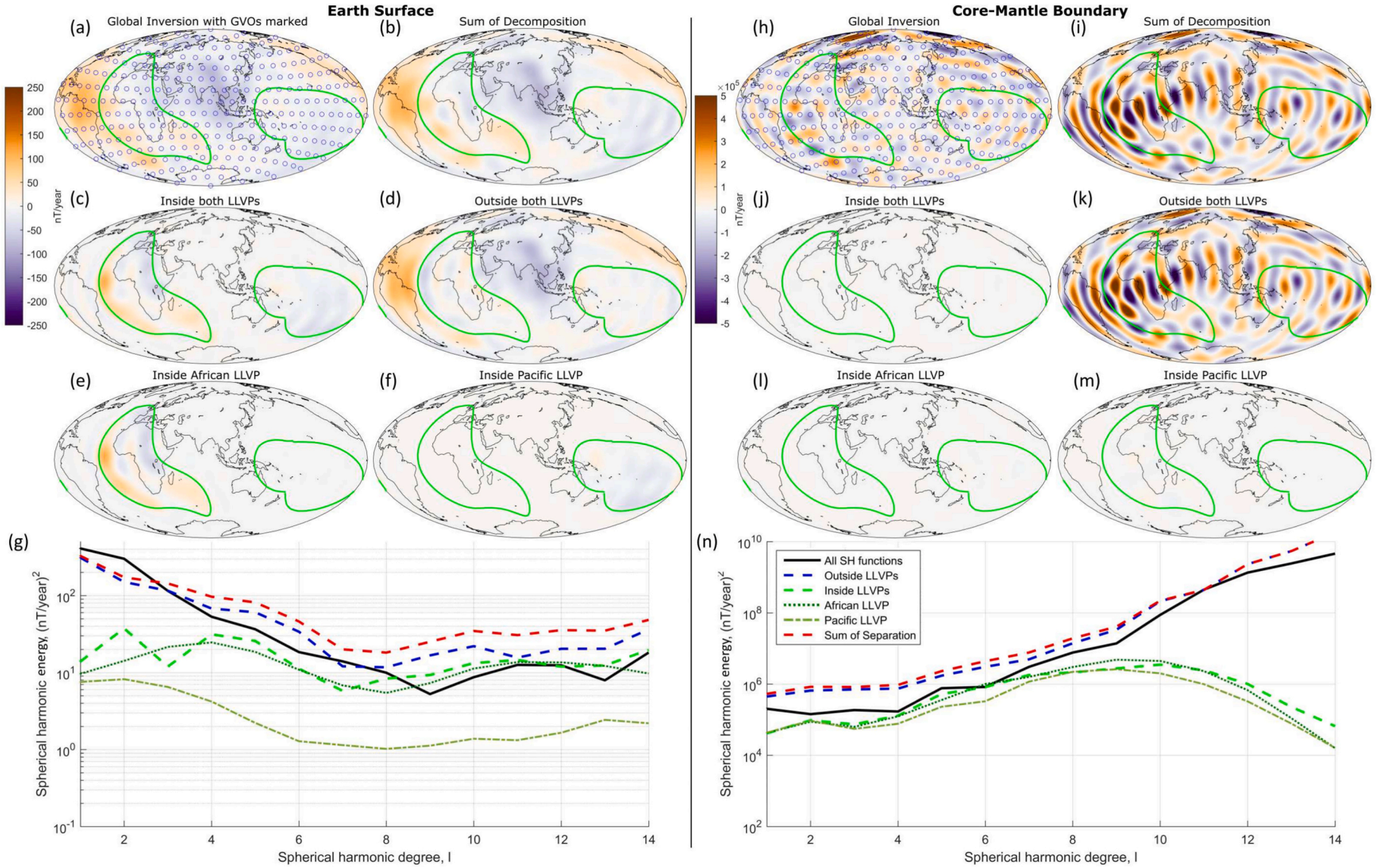

Fig. 3. As for Fig. 2 but for the spherical Slepian separation. Model derived from Swarm GVOs, epoch September 2015. There is almost no signal modeled within the LLVPs for the CMB.

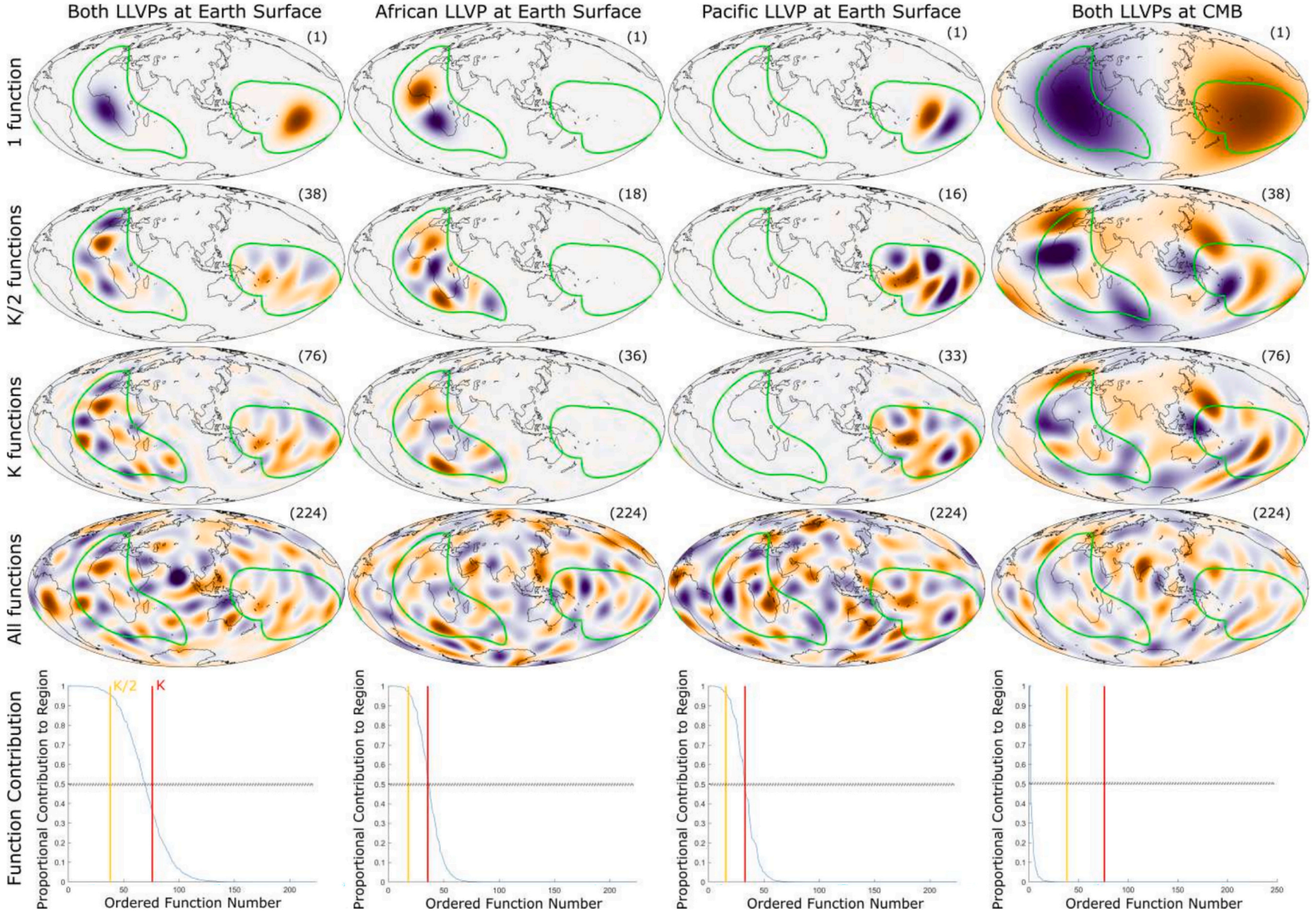

Fig. 4. The spatial patterns of the first (top row), $K/2$ (second row), K (third row) and all of the eigenfunctions (fourth row) in the separations for both LLVPs (column 1), just the African LLVP (column 2), just the Pacific LLVP (column 3) at the Earth's surface and both LLVPs at the CMB in the final column. The final row shows the proportional contribution of each ordered eigenfunction number between 1 and $L(L+2)$ for each case with the K and $K/2$ cut offs shown in red and orange respectively. Intuitively, we would expect a good separation to use all the functions that contribute 50 % (shown in black) or more to the region of interest. (For interpretation of the references to colour in this figure legend, the reader is referred to the web version of this article.)

contribution to the region for each function between 1 and $L(L+2)$. Changing the region area and the shape affects the shape of the proportional energy contribution curve and the resulting choice of K. Adding each additional eigenfunction can have a large effect on the solution, especially in these bandlimited signals.

The final column of Fig. 4 shows the patterns at the CMB for both LLVPs, which can be compared to the first column. The downward continuation to the CMB causes the eigenfunctions to be smeared outside the region edge, so that even the first eigenfunction shows leakage outside the region. This means that very few functions contribute to the patch and instead each eigenfunction has a global footprint. Choosing fewer than 10 functions is not representative of the signal within the region so we have chosen K to be the same as the value used for models at the Earth's surface. The choice of K should be proportional to the surface area of the region but this would mean that our separation has too much signal outside of the region at the Earth's surface. The inversion needs around 130 eigenfunctions to be concentrated inside the region to produce a signal that can be seen on this scale bar and has no features seen in the global spherical harmonic inversion.

6. Regional separation of SV over the satellite era

The same methodology was applied to the separation of GVO data covering the whole satellite era. This gives a time-series of the regional energy at the Earth's surface and CMB, as shown in Fig. 5. The GVO coverage has varied in time and, therefore, we have excluded timesteps where fewer than 90 % of GVOs are available; this occurred often during the early stages of the CHAMP mission and in the gap between CHAMP and Swarm (2010–2014), where some coverage comes from Cryosat-2. The damping parameters, choice of K and bandwidth were kept constant to minimise the number of free parameters and models should reflect only the regional influence affecting SV with the regions. The spherical harmonic spectra are turned into energy values by summing over all degrees.

In Fig. 5, we observe that the patterns identified in the one time step are seen across the entire time-period. The spatial grid methodology is the only methodology for which the energy of the global model is perfectly retrieved by the sum of the separations. The spherical harmonic analysis underestimates the energy and the Slepian overestimates the energy in the separation at the Earth's surface. There is a noticeable jump in energy when changing satellite dataset, demonstrating that the damping should be carefully tuned to the data in the inversion. However, the trade-off if we were to change the damping parameters is that we would not be able to investigate the temporal variation over the LLVP regions as easily. The energy at the CMB is extremely variable from one timestep to the next and may have unwanted annual signals (e.g. ionospheric) within it (Hammer et al., 2021a). During summer months in the southern hemisphere, some GVOs are missing data meaning that the number of GVOs contributing to the SV inversion in January can be reduced by up to 21, leading to poorly constrained inversions. This effect is exaggerated with downward continuation to create large SV energy values at the CMB.

Dividing the regional energy by the global spherical harmonic energy allows for an understanding of the relative importance of different regions, instead of the impact of the methodology. At the Earth's surface, the outside LLVPs region always contributes the greatest percentage ($\approx 85\%$) to the summed composition and the African LLVP contributes about twice the energy of the Pacific LLVP, see Table 2 for exact values. Meanwhile the energy at the CMB for the region outside LLVPs has a lower contribution to the summed composition than at the surface. Interestingly the energy under the LLVPs varies quite a lot, possibly reflecting that magnetic flux patches may be drifting across the region edges and changing the proportion of the SV energy within the region.

A correlation can be seen between the regional proportional energy at the Earth's surface and the timing of jerks (shown in grey in Fig. 5). Jerks are generally described as rapid changes to acceleration of the observed magnetic field field (Mandea et al., 2010). Jerks have been linked to alternating pulses of flow along the CMB with an oscillating signal of either 6 years or 8.6 years (Aubert, 2019; Duan and Huang, 2020). Chulliat and Maus (2014) showed that the secular acceleration has fluctuated as a localised standing wave at the core surface. They also note that the waves are localised in two specific areas (the Atlantic and Indian sectors), which lie within or close to the African LLVP. Meanwhile, jerks that have occurred over the Swarm period (2014–present) have been seen more in the Pacific (Whaler et al., 2022; Pavón-Carrasco et al., 2021), also near a LLVP. While the jerks may happen over a period of a few months, changes in the global acceleration can have a 1 to 3 year delay between the northern and southern hemispheres. Kim and von Frese (2013) applied spherical Slepian functions over spherical caps to investigate jerks in polar regions and found features previously identified; they also confirmed the time lag between jerk observations in the Arctic and Antarctic regions.

The relationship with jerk timings is seen particularly clearly in the separated regions, with inflection points of the separated energy corresponding to jerk timings, especially during the Swarm era. Despite being a consistent feature of the separations at the Earth's surface regardless of methodology, the correlation between inflection points of separated energy and the jerk timings cannot be seen at the CMB. To overcome the limitations arising from the gaps in GVO dataset over the satellite era, we repeat the separation with COV-OBS.x2, a continuous magnetic field model.

7. Regional separation of SV over the era covered by Cov-Obs.x2

The methodology for separating COV-OBS.x2 Gauss coefficients is the same as for the GVO datasets for the pointwise and spherical harmonic methodologies. However, the application of spherical Slepian functions differs. Rather than undertaking an inversion, the COV-OBS.x2 coefficients are separated by applying the $\mathbf{G}$ matrix to them and restricting the number of sorted functions, as shown in Eq. (15). The Slepian methodology we apply here does not recreate the global spherical harmonic inversion because it under-estimates the the energy of the global spherical harmonic solution, particularly at the CMB. Therefore, we put less weight on this technique compared to the other two methodologies. We repeated the separations for the September 2015 timestep of the COV-OBS.x2 model and found the proportional energy of each region is very similar to that obtained from the GVOs ($\leq$ 2% difference) except for the spherical Slepian methodology.

Fig. 6 and Table 3 show many similar features between the results of COV-OBS.x2 and the results from GVOs. The greatest contribution to SV energy is from outside LLVPs, but at the Earth's surface this changes over time from 49 % to 89 %. Although the SV energy under the Pacific LLVP does oscillate, the large decrease in SV energy generated inside the LLVPs is driven by a decrease in SV energy for the African LLVP. The energy at the CMB is more uniform over time but still shows some changes. As with the GVO results, there are strong correlations between geomagnetic jerk timings and the inflection points of the SV energy. As there is no catalogue of 'accepted' jerks, we state that the jerk times we consider are: 1844, 1853, 1862, 1869, 1878, 1888, 1901, 1913, 1924, 1932, 1949, 1969, 1973, 1978, 1984, 1991, 1999, 2004, 2007, 2011, 2014, 2017, 2020 (Mandea et al., 2010; Brown et al., 2013; Qamili et al., 2013; Whaler et al., 2017; Duan and Huang, 2020; Pavón-Carrasco et al., 2021). This correlation is less obvious at the CMB and with the spherical Slepian function methodology.

8. Discussion and conclusion

We can track the westward movement of one positive flux patch from from Australia (1975) to Madagascar (2008) in the COV-OBS.x2 model to estimate the speed at which the SV varies outside and inside the LLVPs. We find that the speed outside the LLVPs is quicker ($\sim 0.6^{\circ}$/year)

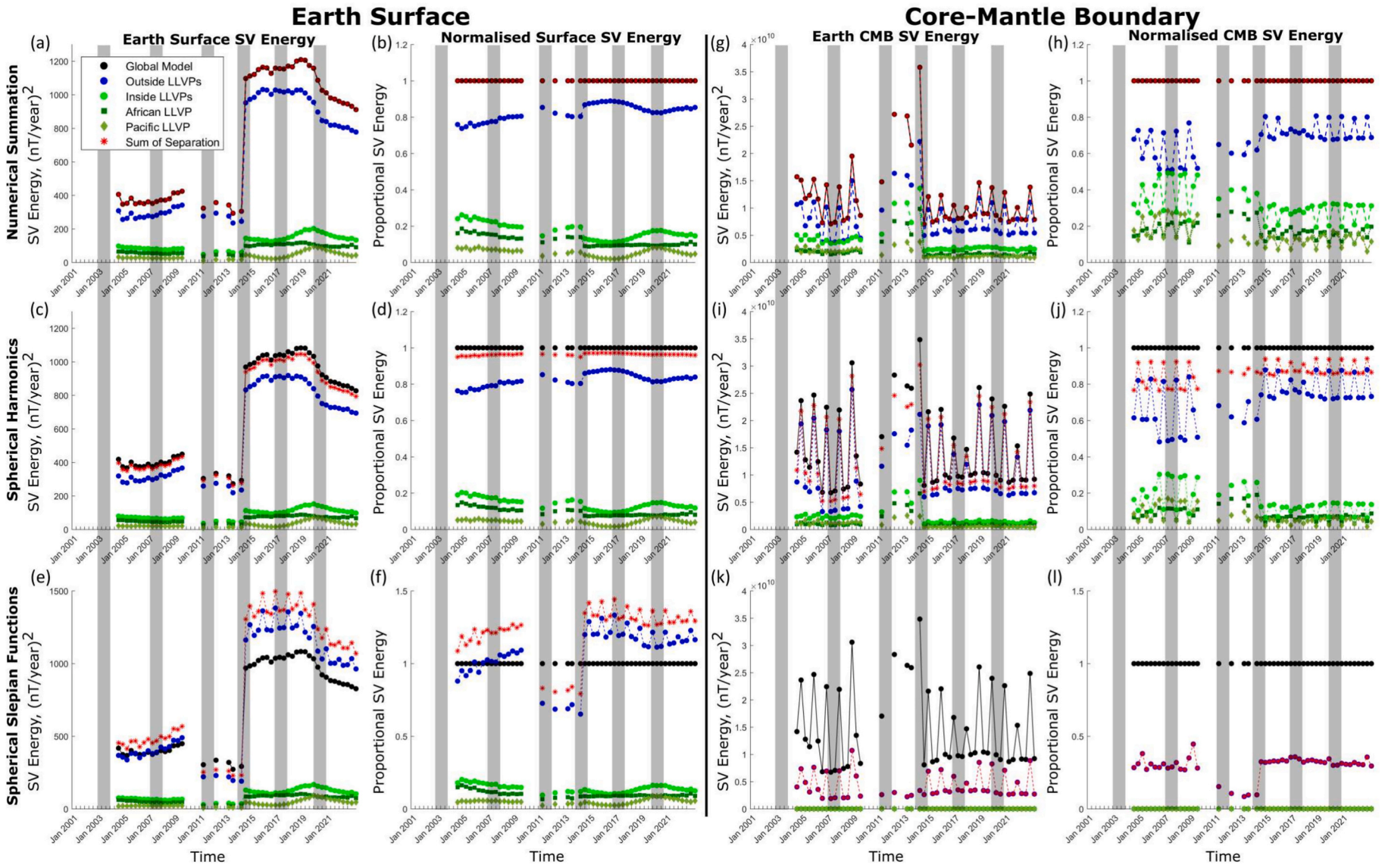

Fig. 5. Energy of the radial secular variation calculated by spatial grid (top), spherical harmonics (middle), and spherical Slepian functions (bottom) for the separated regions using GVO data. The left side shows the energy at the Earth's surface and the right shows the energy at the CMB. In column two and four we normalise the energy by the global spherical harmonic inversion for the Earth's surface and CMB respectively.

Table 2
Proportion of surface area, the average radial SV energy at Earth's surface and the CMB for the separations normalised to the sum of the separation for each of the methodologies derived from GVO data over the satellite era.

EARTH SURFACE	Surface Area	Pointwise	SHA	Slepian
Inside LLVPs	21.8 %	17.4 %	12.3 %	13.3 %
Outside LLVPs	78.2 %	82.6 %	84.3 %	117.3 %
African LLVP	11.9 %	11.8 %	8.3 %	9.3 %
Pacific LLVP	9.9 %	5.5 %	4.0 %	5.1 %

EARTH CMB	Surface Area	Pointwise	SHA	Slepian
Inside LLVPs	21.8 %	32.4 %	14.3 %	<1 %
Outside LLVPs	78.2 %	67.6 %	75.5 %	26.6 %
African LLVP	11.9 %	17.5 %	8.6 %	<1 %
Pacific LLVP	9.9 %	14.9 %	5.3 %	<1 %

compared to that inside them ($\sim 0.45^{\circ}$/year). Both of these values are higher than the average westward drift quoted in the literature (Wei and Xu, 2003; Bullard et al., 1950). Future work could investigate this with more flux patches and over a greater geographical spread, especially as the percentage of SV energy generated under the African LLVP seems to be significantly higher than the Pacific LLVP despite the two LLVPs having a similar surface area. Many other considerations also need to be taken into account including (but not limited to) consistency between different field models, convection bursts, the role of latitude, and the role of waves in moving flux patches.

The lower speed of a flux patch beneath LLVPs and lower proportional SV energy percentage is consistent with LLVPs being hotter than the surrounding mantle, implying lower heat flux across the CMB, thereby suppressing flow underneath them. The resulting field structures could become trapped, minimising the SV generated by advection. 'Hot' LLVPs are expected to suppress small-scale convection (Mound et al., 2019), but there is limited evidence of the SV spectra decreasing at large spherical harmonic degrees (small-spatial scales) in Figs. 3(g and n) and 2(g). Nevertheless, LLVPs being hotter than the surrounding mantle is not a unique explanation for slower flux patch speed as enhanced electrical conductivity in LLVPs could increase electromagnetic drag on the fluid or provide a masking of the SV as it is upward continued to the surface (Holme, 2000; Schaeffer and Jault, 2016; Dumberry and More, 2020; Matsushima, 2020). There is no clear link between our results and physical parameters, especially as the energy inside the LLVPs at the Earth's surface is found to be proportionally higher than the surface area when separating COV-OBS.x2 coefficients but lower than the surface area when inverting from GVOs regardless of the methodology. The difference between SV energy advection under the two LLVPs could be an indicator of the LLVPs having different composition, temperature, or evolution (e.g Panton et al., 2025) or we could be capturing the broader quasi-hemispheric pattern of low SV across the whole Pacific relative to the rest of the world (e.g Mound et al., 2015).

We have found that the SV energy spectra for inside and outside LLVPs show rapid changes at times that correspond with jerks. The jerks can be identified in all spherical harmonic degrees, show no difference in the degrees related to antipodal structures ($l = 2$ and 4), and can be seen inside and outside the LLVPs. Possible reasons for this correlation include: (1) the LLVPs (and their lower CMB heat flux) provide a longitudinal preference for geomagnetic jerks, or (2) the effect of sampling a time-varying signal at antipodal locations beneath the LLVPs, or (3) a different mantle filter for above LLVPs compared to elsewhere (Dumberry and More, 2020). We cannot further comment on this without a better regional methodology to investigate geomagnetic jerk occurrence.

The spherical Slepian function methodology is dependent on the region outline and, thus, explains why our solutions for both LLVPs are different from those for individual LLVPs. Fig. 4 shows that the sum of all eigenfunctions at the Earth's surface is different for a decomposition of both LLVPs and when they are considered individually, suggesting that the maximum spherical harmonic degree is not large enough to converge to a common solution. Despite the differences in the Slepian eigenfunctions depending on whether the LLVPs are treated as individual or joint regions, the global spherical harmonic solution is perfectly recreated regardless of which separation is considered. This is curious and demonstrates our incomplete understanding of exactly how the spherical Slepian methodology works. In particular, the applicability of altitude-cognizant spherical Slepian functions at extreme downward continuation ratios needs to be explored further.

While this study has demonstrated that SV is not systematically suppressed under the footprint of LLVPs, further research is needed to understand the detailed reasons for the differences between the inversions of GVO SV and COV-OBS.x2 and the decline in the contribution to SV beneath LLVPs over the last century. A comparison between the methodologies shows that none of them perform ideally in terms of field separation, and the separation of an existing spherical harmonic model gives different results to those from inverting data for a model of SV inside and outside the LLVPs. This frustrates our ability to investigate the underlying hypothesis that there are differences in the behaviour of the magnetic field in these regions in response to thermal or other geophysical parameters. Some future considerations to build on our findings include:

- investigating the difference in core surface flow energy beneath LLVPs compared to outside them in only the equatorial band. It is believed that different dynamics are operating in different parts of the core, such as inside and outside the projection of the cylinder tangent to the inner core onto the CMB, so looking at longitudinal influence in the equatorial band may be more indicative.
- investigating why the Pacific and African LLVPs appear to have extremely different influence on the SV and hence the core flow underneath them. This has been linked to the height of the LLVP above the CMB (Yuan and Li, 2022a, 2022b) or its evolutionary history (Panton et al., 2025) but further multi-disciplinary work needs to be undertaken.
- repeating the separations with different region outlines to encompass outlines proposed by different seismology models. A smoother LLVP shape (e.g. a circle or ellipse) would improve the separation with the Slepian approach but may not capture the true nature of the region.
- improvements to treating the damping in the spherical Slepian inversions - the damping currently applied in our inversion is global, consistent between timesteps, and may not be the most appropriate.
- ensuring that a value for λ is chosen independently for each satellite in GVO inversions. We have kept this constant to reduce the number of free parameters but Fig. 5 shows a noticeable jump when changing satellite dataset.
- adapting appropriate methodologies to complete local inversions from a global dataset – we have presented three methodologies but each has been shown here to have limitations.
- attempting regional investigations of SV approximated at the CMB using new techniques, as our investigations show that the large downward continuation and the limited bandwidth of the signal limit the effectiveness of our methodology. Future developments of the Subtractive Optimally Localised Averages (SOLA) methodology (Hammer et al., 2021b) may help to overcome this.

In this study, we have investigated the effects of the LLVPs on the magnetic field without assuming any physical property values (e.g. heat flux differences) of the LLVPs from other disciplines. This work demonstrates that we can estimate the proportion of SV energy generated under the LLVPs and find that the area outside the LLVPs makes the largest contribution (and larger than expected) to SV. At the Earth's surface, the African LLVP contributes approximately three times the amount of SV energy as the Pacific LLVP but only around 1.3 times more

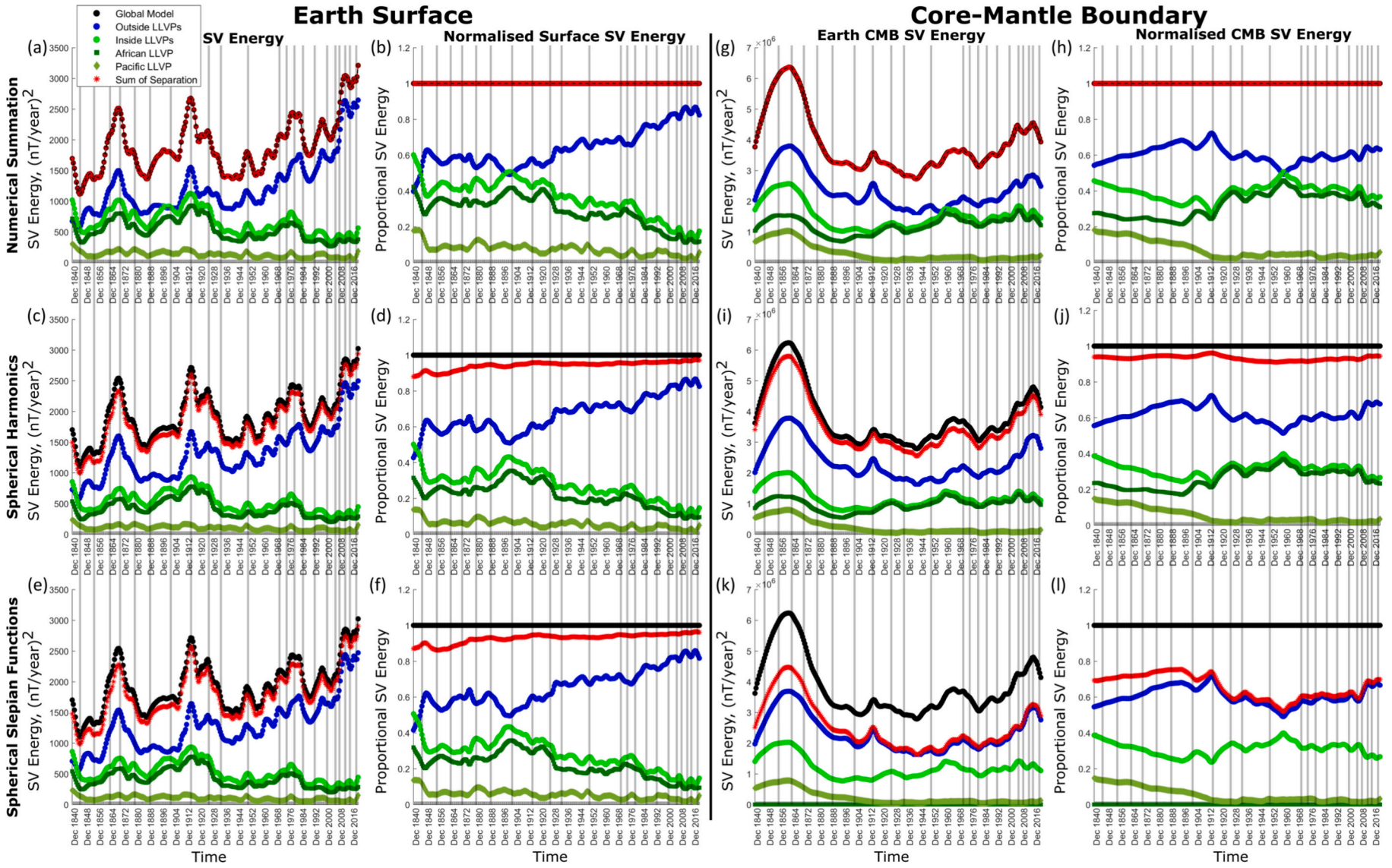

Fig. 6. Proportion of surface area, the average radial SV energy at Earth's surface and the CMB for the separations normalised to the sum of the separation for each of the methodologies utilising COV-OBS.x2.

Table 3
Proportion of surface area, the average radial SV energy at Earth's surface and the CMB for the separations normalised to the sum of the separation for each of the methodologies derived using the COV-OBS.x2 coefficients.

EARTH SURFACE	Surface Area	Pointwise	SHA	Slepian
Inside LLVPs	21.8 %	36.1 %	29.9 %	30.5 %
Outside LLVPs	78.2 %	63.9 %	70.7 %	70.2 %
African LLVP	11.9 %	28.7 %	23.3 %	23.8 %
Pacific LLVP	9.9 %	7.5 %	6.1 %	6.0 %

EARTH CMB	Surface Area	Pointwise	SHA	Slepian
Inside LLVPs	21.8 %	39.5 %	33.6 %	48.5 %
Outside LLVPs	78.2 %	60.5 %	66.4 %	92.4 %
African LLVP	11.9 %	32.2 %	27.9 %	<1 %
Pacific LLVP	9.9 %	7.3 %	5.7 %	7.6 %

energy at the CMB. We can have some confidence in our findings as there is good agreement in the decomposition for all three methodologies over the GVO satellite era (September 2006–June 2020) and for the period covered by the COV-OBS.x2 model (1880–2020). All models at Earth's surface show decadal fluctuations in proportional LLVP energy with a trend towards a lower proportion of LLVP SV energy over the last century. We conclude that LLVPs do show varying SV with time under their footprint and, therefore, rather than being regions of stilted or negligible flow, core flow varies significantly underneath them over time.

CRediT authorship contribution statement

Hannah F. Rogers: Writing – review & editing, Writing – original draft, Methodology, Formal analysis. **Ciarán D. Beggan:** Writing – review & editing, Supervision, Methodology, Conceptualization. **Kathryn A. Whaler:** Writing – review & editing, Supervision, Methodology, Conceptualization.

Declaration of competing interest

The authors declare that they have no known competing financial interests or personal relationships that could have appeared to influence the work reported in this paper.

Acknowledgments

The authors wish to thank Frederik Simons and Alain Plattner for their advice and support in adapting spherical Slepian functions for this purpose. This would not have been possible without access to their publically available code. We also acknowledge stimulating conversations with Cathy Constable during a visit to IGPP.

The majority of this work was undertaken when HR was funded through the E3 DTP at the University of Edinburgh by NERC grant NE/L002558/1, and a NERC CASE studentship with a British Geological Survey BUFI grant (BGS contract GA/17S/009). This work was written up while HR was funded by the European Research Council (ERC) under the European Union's Horizon 2020 research and innovation programme (GRACEFUL Synergy Grant agreement No 855677). HR is part of Labex OSUG@2020 (ANR10 LABX56). Corrections were undertaken when HR recieved funding from Natural Environment Research Council grant NE/V010867/1.

Data availability

The spherical Slepian code (doi: https://doi.org/10.1137/S0036144504445765) is available from: https://geoweb.princeton.edu/people/simons/software.html.

The GVO dataset is available from: https://www.space.dtu.dk/english/research-divisions/geomagnetism-and-geospace/projects/geomagnetic-virtual-observatories

The COV-OBS.x2 model is available from (Huder et al., 2020): https://geodyn.univ-grenoble-alpes.fr/

Please contact authors for access to the SV inversion code.

References

Alken, P., Thébault, E., Beggan, C.D., Amit, H., Aubert, J., Baerenzung, J., Bondar, T.N., Brown, W.J., Califf, S., Chambodut, A., Chulliat, A., Cox, G.A., Finlay, C.C., Fournier, A., Gillet, N., Grayver, A., Hammer, M.D., Holschneider, M., Huder, L., Hulot, G., Jager, T., Kloss, C., Korte, M., Kuang, W., Kuvshinov, A., Langlais, B., Léger, J.M., Lesur, V., Livermore, P.W., Lowes, F.J., Macmillan, S., Magnes, W., Mandea, M., Marsal, S., Matzka, J., Metman, M.C., Minami, T., Morschhauser, A., Mound, J.E., Nair, M., Nakano, S., Olsen, N., Pavón-Carrasco, F.J., Petrov, V.G., Ropp, G., Rother, M., Sabaka, T.J., Sanchez, S., Saturnino, D., Schnepf, N.R., Shen, X., Stolle, C., Tangborn, A., Tøffner-Clausen, L., Toh, H., Torta, J.M., Varner, J., Vervelidou, F., Vigneron, P., Wardinski, I., Wicht, J., Woods, A., Yang, Y., Zeren, Z., Zhou, B., 2021a. International geomagnetic reference field: the thirteenth generation. Earth Planets Space 73, 49. https://doi.org/10.1186/s40623-020-01288-x.

Alken, P., Thébault, E., Beggan, C.D., Aubert, J., Baerenzung, J., Brown, W.J., Califf, S., Chulliat, A., Cox, G.A., Finlay, C.C., Fournier, A., Gillet, N., Hammer, M.D., Holschneider, M., Hulot, G., Korte, M., Lesur, V., Livermore, P.W., Lowes, F.J., Macmillan, S., Nair, M., Olsen, N., Ropp, G., Rother, M., Schnepf, N.R., Stolle, C., Toh, H., Vervelidou, F., Vigneron, P., Wardinski, I., 2021b. Evaluation of candidate models for the 13th generation international geomagnetic reference field. Earth Planets Space 73, 48. https://doi.org/10.1186/s40623-020-01281-4.

Amit, H., Choblet, G., Olson, P., Monteux, J., Deschamps, F., Langlais, B., Tobie, G., 2015. Towards more realistic core-mantle boundary heat flux patterns: a source of diversity in planetary dynamos. Progress in earth and planetary. Science 2, 26. URL. http://www.progearthplanetsci.com/content/2/1/26. https://doi.org/10.1186/s40645-015-0056-3.

Aubert, J., 2019. Approaching earth's core conditions in high-resolution geodynamo simulations. Geophys. J. Int. 219, S137–S151. https://doi.org/10.1093/gji/ggz232.

Baerenzung, J., Holschneider, M., Lesur, V., 2016. The flow at the earth's core-mantle boundary under weak prior constraints. J. Geophys. Res. Solid Earth 121, 1343–1364. https://doi.org/10.1002/2015JB012464.

Barrois, O., Hammer, M.D., Finlay, C.C., Martin, Y., Gillet, N., 2018. Assimilation of ground and satellite magnetic measurements: inference of core surface magnetic and velocity field changes. Geophys. J. Int. 215, 695–712. https://doi.org/10.1093/gji/ggy297.

Beggan, C., Whaler, K., 2008. Core flow modelling assumptions. Phys. Earth Planet. In. 167, 217–222.

Beggan, C.D., Saarimäki, J., Whaler, K.A., Simons, F.J., 2013. Spectral and spatial decomposition of lithospheric magnetic field models using spherical slepian functions. Geophys. J. Int. 193, 136–148. https://doi.org/10.1093/gji/ggs122.

Brown, W., Mound, J., Livermore, P., 2013. Jerks abound: an analysis of geomagnetic observatory data from 1957 to 2008. Phys. Earth Planet. In. 223, 62–76. https://doi.org/10.1016/j.pepi.2013.06.001.

Bullard, E.C., Freedman, C., Gellman, H., Nixon, J., 1950. The westward drift of the earth's magnetic field. Philos. Trans. R. Soc. Lond. 243, 67–91.

Chulliat, A., Maus, S., 2014. Geomagnetic secular acceleration, jerks, and a localized standing wave at the core surface from 2000 to 2010. J. Geophys. Res. Solid Earth 119, 1531–1543. https://doi.org/10.1002/2013JB010604.

Dahlen, F.A., Simons, F.J., 2008. Spectral estimation on a sphere in geophysics and cosmology. Geophys. J. Int. 174, 774–807. https://doi.org/10.1111/j.1365-246X.2008.03854.x.

Dahlen, F.A., Tromp, J., 1998. Theoretical Global Seismology. Princeton University Press, Princeton.

Davies, C.J., Gubbins, D., Willis, A.P., Jimack, P.K., 2008. Time-averaged paleomagnetic field and secular variation: predictions from dynamo solutions based on lower mantle seismic tomography. Phys. Earth Planet. In. 169, 194–203. https://doi.org/10.1016/j.pepi.2008.07.021.

Doubrovine, P.V., Steinberger, B., Torsvik, T.H., 2016. A failure to reject: testing the correlation between large igneous provinces and deep mantle structures with EDF statistics. Geochem. Geophys. Geosyst. 17, 1130–1163. https://doi.org/10.1002/2015GC006044.

Duan, P., Huang, C., 2020. Intradecadal variations in length of day and their correspondence with geomagnetic jerks. Nat. Commun. 11, 2273. https://doi.org/10.1038/s41467-020-16109-8.

Dumberry, M., More, C., 2020. Weak magnetic field changes over the Pacific due to high conductance in lowermost mantle. Nat. Geosci. 13, 516–520. https://doi.org/10.1038/s41561-020-0589-y.

Engbers, Y.A., Biggin, A.J., Bono, R.K., 2020. Elevated paleomagnetic dispersion at Saint Helena suggests long-lived anomalous behavior in the South Atlantic. Proc. Natl. Acad. Sci. 117, 18258–18263. https://doi.org/10.1073/pnas.2001217117.

Finlay, C.C., Kloss, C., Olsen, N., Hammer, M.D., Tøffner-Clausen, L., Grayver, A., Kuvshinov, A., 2020. The CHAOS-7 geomagnetic field model and observed changes in the South Atlantic anomaly. Earth Planets Space 72. https://doi.org/10.1186/s40623-020-01252-9.

Frost, D.A., Rost, S., 2014. The P-wave boundary of the large-low shear Velocity Province beneath the Pacific. Earth Planet. Sci. Lett. 403, 380–392. https://doi.org/10.1016/j.epsl.2014.06.046.

Garnero, E.J., Kennett, B., Loper, D.E., 2005. Studies of the earth's deep interior—eighth symposium. Phys. Earth Planet. In. 153, 1–2. https://doi.org/10.1016/j.pepi.2005.08.003.
Garnero, E., McNamara, A.K., Shim, S.H., 2016. Continent-sized anomalous zones with low seismic velocity at the base of earth's mantle. Nat. Geosci. 9, 481–489. https://doi.org/10.1038/ngeo2733.
Gibbons, S.J., Gubbins, D., 2000. Convection in the earth's core driven by lateral variations in the core-mantle boundary heat flux. Geophys. J. Int. 142, 631–642. https://doi.org/10.1046/j.1365-246x.2000.00192.x.
Glatzmaier, G.A., Coe, R.S., Hongre, L., Roberts, P.H., 1999. The role of the earth's mantle in controlling the frequency of geomagnetic reversals. Nature 401, 885–890. https://doi.org/10.1038/44776.
Gubbins, D., Willis, A.P., Sreenivasan, B., 2007. Correlation of earth's magnetic field with lower mantle thermal and seismic structure. Phys. Earth Planet. In. 162, 256–260. https://doi.org/10.1016/j.pepi.2007.04.014.
Hammer, M.D., Cox, G.A., Brown, W.J., Beggan, C.D., Finlay, C.C., 2021a. Geomagnetic virtual observatories: monitoring geomagnetic secular variation with the swarm satellites. Earth Planets Space 73. https://doi.org/10.1186/s40623-021-01357-9.
Hammer, M.D., Finlay, C.C., Olsen, N., 2021b. Applications for CryoSat-2 satellite magnetic data in studies of earth's core field variations. Earth Planets Space 73, 73. https://doi.org/10.1186/s40623-021-01365-9.
Harig, C., Simons, F.J., 2012. Mapping Greenland's mass loss in space and time. Proc. Natl. Acad. Sci. 109, 19934–19937. https://doi.org/10.1073/pnas.1206785109.
Heyn, B.H., Conrad, C.P., Trønnes, R.G., 2020. Core-mantle boundary topography and its relation to the viscosity structure of the lowermost mantle. Earth Planet. Sci. Lett. 543, 116358. https://doi.org/10.1016/j.epsl.2020.116358.
Holme, R., 2000. Electromagnetic core–mantle coupling: III. Laterally varying mantle conductance. Phys. Earth Planet. In. 117, 329–344. https://doi.org/10.1016/S0031-9201(99)00105-3.
Holme, R., 2007. Length of day variations, decadal. In: Gubbins, D., Herrero-Bervera, E. (Eds.), Encyclopedia of Geomagnetism and Paleomagnetism. Springer, Netherlands, Dordrecht, pp. 469–470. https://doi.org/10.1007/978-1-4020-4423-6{_}167.
Holme, R., 2015. Large-Scale Flow in the Core, vol. 8. Elsevier B.V. https://doi.org/10.1016/B978-0-444-53802-4.00138-X. URL.
Huder, L., Gillet, N., Finlay, C.C., Hammer, M.D., Tchoungui, H., 2020. COV-OBS.x2: 180 years of geomagnetic field evolution from ground-based and satellite observations. Earth Planets Space 72, 160. https://doi.org/10.1186/s40623-020-01194-2.
Jault, D., Gire, C., Le Mouel, J.L., 1988. Westward drift, core motions and exchanges of angular momentum between core and mantle. Nature 333, 353–356. https://doi.org/10.1038/333353a0.
Kellogg, L.H., Hager, B.H., van der Hilst, R.D., 1999. Compositional stratification in the deep mantle. Science 283, 1881–1884. https://doi.org/10.1126/science.283.5409.1881.
Kim, H.R., von Frese, R.R.B., 2013. Localized analysis of polar geomagnetic jerks. Tectonophysics 585, 26–33. https://doi.org/10.1016/j.tecto.2012.06.038.
Kim, H.R., von Frese, R.R.B., 2017. Utility of Slepian basis functions for modeling near-surface and satellite magnetic anomalies of the Australian lithosphere. Earth Planets Space 69, 53. URL: http://earth-planets-space.springeropen.com/articles/10.1186/s40623-017-0636-0 https://doi.org/10.1186/s40623-017-0636-0.
Kloss, C., Finlay, C.C., 2019. Time-dependent low-latitude core flow and geomagnetic field acceleration pulses. Geophys. J. Int. 217, 140–168. URL: doi:https://doi.org/10.1093/gji/ggy545, doi:https://doi.org/10.1093/gji/ggy545.
Koelemeijer, P., 2021. Toward consistent seismological models of the core–mantle boundary landscape. In: Marquardt, H., Ballmer, M., Cottaar, S., Konter, J. (Eds.), Mantle Convection and Surface Expressions, Geophysical Monograph 263, first ed. John Wiley & Sons Inc., pp. 229–255. https://doi.org/10.1002/9781119528609.ch9
Labrosse, S., Hernlund, J.W., Coltice, N., 2007. A crystallizing dense magma ocean at the base of the earth's mantle. Nature 450, 866–869. https://doi.org/10.1038/nature06355.
Livermore, P., Hollerbach, R., Finlay, C., 2016. An accelerating high-latitude jet in earth's core. Nat. Geosci. 10, 62–68. http://www.nature.com/doifinder/10.1038/ngeo2859. https://doi.org/10.1038/ngeo2859.
Lowes, F.J., 1966. Mean-square values on sphere of spherical harmonic vector fields. J. Geophys. Res. 71, 2179. URL. https://doi.org/10.1029/JZ071i008p02179.
Ma, X., Tkalčić, H., 2024. Seismic low-velocity equatorial torus in the earth's outer core: evidence from the late–coda correlation wavefield. Sci. Adv. 10. https://doi.org/10.1126/sciadv.adn5562.
Mandea, M., Olsen, N., 2006. A new approach to directly determine the secular variation from magnetic satellite observations. Geophys. Res. Lett. 33, 1–5. https://doi.org/10.1029/2006GL026616.
Mandea, M., Holme, R., Pais, A., Pinheiro, K., Jackson, A., Verbanac, G., 2010. Geomagnetic jerks: rapid Core field variations and Core dynamics. Space Sci. Rev. 155, 147–175. https://doi.org/10.1007/s11214-010-9663-x.
Matsushima, M., 2020. Effect of core electrical conductivity on core surface flow models. Earth Planets Space 72, 180. https://doi.org/10.1186/s40623-020-01269-0.
Mauersberger, P., 1956. Das Mittel der Energiedichte des geomagnetischen Hauptfeldes an der Erdoberfläche und seine säkulare Änderung. Gerlands Beitrage Geophysik 65, 207–215.
Maus, S., 2008. The geomagnetic power spectrum. Geophys. J. Int. 174, 135–142. https://doi.org/10.1111/j.1365-246X.2008.03820.x.
McNamara, A.K., 2019. A review of large low shear velocity provinces and ultra low velocity zones. Tectonophysics 760, 199–220. https://doi.org/10.1016/j.tecto.2018.04.015.
Mound, J.E., Davies, C.J., 2023. Longitudinal structure of earth's magnetic field controlled by lower mantle heat flow. Nat. Geosci. https://doi.org/10.1038/s41561-023-01148-9.
Mound, J., Davies, C., Silva, L., 2015. Inner core translation and the hemispheric balance of the geomagnetic field. Earth Planet. Sci. Lett. 424, 148–157. https://doi.org/10.1016/j.epsl.2015.05.028.
Mound, J., Davies, C., Rost, S., Aurnou, J., 2019. Regional stratification at the top of earth's core due to core–mantle boundary heat flux variations. Nat. Geosci. 12, 575–580. https://doi.org/10.1038/s41561-019-0381-z.
Niu, Y., 2018. Origin of the LLSVPs at the base of the mantle is a consequence of plate tectonics – a petrological and geochemical perspective. Geosci. Front. 9, 1265–1278. https://doi.org/10.1016/j.gsf.2018.03.005.
Olson, P., 2016. Mantle control of the geodynamo: consequences of top-down regulation. Geochem. Geophys. Geosyst. 17, 1935–1956. https://doi.org/10.1002/2016GC006334.
Panton, J., Davies, J.H., Koelemeijer, P., Myhill, R., Ritsema, J., 2025. Unique composition and evolutionary histories of large low velocity provinces. Sci. Rep. 15, 4466. https://doi.org/10.1038/s41598-025-88931-3.
Pavón-Carrasco, F.J., Marsal, S., Campuzano, S.A., Torta, J.M., 2021. Signs of a new geomagnetic jerk between 2019 and 2020 from swarm and observatory data. Earth Planets Space 73, 175. https://doi.org/10.1186/s40623-021-01504-2.
Plattner, A.M., Johnson, C.L., 2021. Mercury's northern rise Core-field magnetic anomaly. Geophys. Res. Lett. 48. https://doi.org/10.1029/2021GL094695.
Plattner, A., Simons, F.J., 2015. High-resolution local magnetic field models for the Martian south Pole from Mars global surveyor data. Journal of Geophysical Research E: Planets 120, 1543–1566. URL. https://agupubs.onlinelibrary.wiley.com/doi/abs/10.1002/2015JE004869. https://doi.org/10.1002/2015JE004869.
Qamili, E., De Santis, A., Isac, A., Mandea, M., Duka, B., Simonyan, A., 2013. Geomagnetic jerks as chaotic fluctuations of the earth's magnetic field. Geochem. Geophys. Geosyst. 14, 839–850. https://doi.org/10.1029/2012GC004398.
Richards, F.D., Hoggard, M.J., Ghelichkhan, S., Koelemeijer, P., Lau, H.C., 2023. Geodynamic, geodetic, and seismic constraints favour deflated and dense-cored LLVPs. Earth Planet. Sci. Lett. 602, 117964. https://doi.org/10.1016/j.epsl.2022.117964.
Ritsema, J., Deuss, A., van Heijst, H.J., Woodhouse, J.H., 2011. S40RTS: a degree-40 shear-velocity model for the mantle from new Rayleigh wave dispersion, teleseismic traveltime and normal-mode splitting function measurements. Geophys. J. Int. 184, 1223–1236. https://doi.org/10.1111/j.1365-246X.2010.04884.x.
Rogers, H.F., Beggan, C.D., Whaler, K.A., 2019. Investigation of regional variation in core flow models using spherical Slepian functions. Earth Planets Space 71, 19. https://doi.org/10.1186/s40623-019-0997-7.
Schaeffer, N., Jault, D., 2016. Electrical conductivity of the lowermost mantle explains absorption of core torsional waves at the equator. Geophys. Res. Lett. 43, 4922–4928. https://doi.org/10.1002/2016GL068301.
Simons, F.J., 2010. Slepian functions and their use in signal estimation and spectral analysis. In: Freeden, W., Nashed, M.Z., Sonar, T. (Eds.), Handbook of Geomathematics. Springer, Berlin Heidelberg, Berlin, Heidelberg, pp. 891–923. https://doi.org/10.1007/978-3-642-01546-5_30.
Simons, F.J., Dahlen, F.A., Wieczorek, M.A., 2006. Spatiospectral concentration on a sphere. SIAM Rev. 48, 504–536. URL. http://epubs.siam.org/doi/abs/10.1137/S0036144504445765. https://doi.org/10.1137/S0036144504445765.
Simons, F., Hawthorne, C., Beggan, D., 2009. Efficient analysis and representation of geophysical processes using localized spherical basis functions. Proc. SPIE-Int. Soc. Opt. Eng. 7446. https://doi.org/10.1117/12.825730.
Tarduno, J.A., Watkeys, M.K., Huffman, T.N., Cottrell, R.D., Blackman, E.G., Wendt, A., Scribner, C.A., Wagner, C.L., 2015. Antiquity of the South Atlantic anomaly and evidence for top-down control on the geodynamo. Nat. Commun. 6, 7865. https://doi.org/10.1038/ncomms8865.
Terra-Nova, F., Amit, H., 2024. Regionally-triggered geomagnetic reversals. Scientific Reports 14, 9639. https://doi.org/10.1038/s41598-024-59849-z.
Torsvik, T.H., Burke, K., Steinberger, B., Webb, S.J., Ashwal, L.D., 2010. Diamonds sampled by plumes from the core–mantle boundary. Nature 466, 352–355. https://doi.org/10.1038/nature09216.
Torsvik, T.H., van der Voo, R., Doubrovine, P.V., Burke, K., Steinberger, B., Ashwal, L.D., Tronnes, R.G., Webb, S.J., Bull, A.L., 2014. Deep mantle structure as a reference frame for movements in and on the earth. Proc. Natl. Acad. Sci. 111, 8735–8740. https://doi.org/10.1073/pnas.1318135111.
van Tent, R., Deuss, A., Kaneshima, S., Thomas, C., 2020. The signal of outermost-core stratification in body-wave and normal-mode data. Geophys. J. Int. 223, 1338–1354. https://doi.org/10.1093/gji/ggaa368.
Wang, W., Xu, Y., Sun, D., Ni, S., Wentzcovitch, R., Wu, Z., 2020. Velocity and density characteristics of subducted oceanic crust and the origin of lower-mantle heterogeneities. Nat. Commun. 11, 64. https://doi.org/10.1038/s41467-019-13720-2.
Wei, Z.G., Xu, W.Y., 2003. Westward drift in secular variation of the main geomagnetic field inferred from IGRF. Earth Planets Space 55, 131–137. https://doi.org/10.1186/BF03351740.
Whaler, K., Hammer, M., Finlay, C.C., Olsen, N., 2017. Probing the core surface flow with satellite data. In: IAPSO-IAMAS-IAGA Joint Assembly Cape Town, p. 651. URL.

http://iapso.iugg.org/scientific-assemblies23/79-2017-iapso-iamas-iaga-joint-assembly.html.
Whaler, K.A., Hammer, M.D., Finlay, C.C., Olsen, N., 2022. Core surface flow changes associated with the 2017 Pacific geomagnetic jerk. Geophys. Res. Lett. 49. https://doi.org/10.1029/2022GL098616.
Winch, D., 2007. Harmonics, spherical. In: Gubbins, D., Herro-Bervera, E. (Eds.), Encyclopedia of Geomagnetism and Paleomagnetism. Springer, Netherlands, Dordrecht, pp. 377–394. https://doi.org/10.1007/978-1-4020-4423-6{_}135.
Yuan, Q., Li, M., 2022a. Instability of the African large low-shear-wave-velocity province due to its low intrinsic density. Nat. Geosci. 15, 334–339. https://doi.org/10.1038/s41561-022-00908-3.
Yuan, Q., Li, M., 2022b. Vastly Different Heights of LLVPs caused by different strengths of historical slab push. Geophys. Res. Lett. 49. https://doi.org/10.1029/2022GL099564.
Yuan, Q., Li, M., Desch, S.J., Ko, B., Deng, H., Garnero, E.J., Gabriel, T.S.J., Kegerreis, J. A., Miyazaki, Y., Eke, V., Asimow, P.D., 2023. Moon-forming impactor as a source of earth's basal mantle anomalies. Nature 623, 95–99. https://doi.org/10.1038/s41586-023-06589-1.
Zhang, K., Gubbins, D., 1992. On convection in the earth's core driven by lateral temperature variations in the lower mantle. Geophys. J. Int. 108, 247–255. https://doi.org/10.1111/j.1365-246X.1992.tb00853.x.